CHALMERS
UNIVERSITY OF TECHNOLOGY

Implementing intermittent current interruption into Li-ion cell modelling for improved battery diagnostics

Downloaded from: https://research.chalmers.se, 2024-04-23 06:30 UTC

Citation for the original published paper (version of record):
Yin, L., Geng, Z., Chien, Y. et al (2022). Implementing intermittent current interruption into Li-ion cell modelling for improved battery
diagnostics. Electrochimica Acta, 427. http://dx.doi.org/10.1016/j.electacta.2022.140888

N.B. When citing this work, cite the original published paper.

research.chalmers.se offers the possibility of retrieving research publications produced at Chalmers University of Technology.
It covers all kind of research output: articles, dissertations, conference papers, reports etc. since 2004.
research.chalmers.se is administrated and maintained by Chalmers Library

(article starts on next page)

Electrochimica Acta 427 (2022) 140888

Contents lists available at ScienceDirect

Electrochimica Acta

journal homepage: www.journals.elsevier.com/electrochimica-acta

Implementing intermittent current interruption into Li-ion cell modelling for improved battery diagnostics

Litao Yin [a], Zeyang Geng [b], Yu-Chuan Chien [a], Torbjörn Thiringer [b], Matthew J. Lacey [c], Anna M. Andersson [d], Daniel Brandell [a,*]

[a] Department of Chemistry - Ångström Laboratory, Uppsala University, Uppsala 751 21, Sweden
[b] Department of Electrical Engineering, Division of Electric Power Engineering, Chalmers University of Technology, S-412 96 Göteborg, Sweden
[c] Scania CV AB, Södertälje 15187, Sweden
[d] ABB AB Corporate Research, Forskargränd 7, Västerås SE-721 78, Sweden

ARTICLE INFO

Keywords:
Li-ion battery
Physics-based model
Intermittent current interruption
Resistance mapping
Battery diagnostic

ABSTRACT

A novel electroanalytical method, the intermittent current interruption (ICI) technique, has recently been promoted as a versatile tool for battery analysis and diagnostics. The technique enables frequent and continuous measurement of battery resistance, which then undergoes statistical analysis. Here, this method is implemented for commercial Li-ion cylindrical cells, and combined with a physics-based finite element model (FEM) of the battery to better interpret the measured resistances. Ageing phenomena such as solid electrolyte interphase (SEI) formation and metallic Li plating on the surface of the negative graphite particles are considered in the model. After validation, a long-term cycling simulation is conducted to mimic the ageing scenario of commercial cylindrical 21700 cells. The large number of internal resistance measurements obtained are subsequently visualized by creating a 'resistance map' as a function of both capacity and cycle numbers, providing a straight-forward image of their continuous evolution. By correlating the observed ageing scenarios with specific physical processes, the origins of ageing are investigated. The result shows that a decrease of the electrolyte volume fraction contributes significantly to the increase of internal resistance and affect the electrolyte diffusivity properties. Additionally, effects of porosity and particle radius of the different electrodes are investigated, providing valuable suggestions for battery design.

1. Introduction

The rapidly growing demands on energy storage for grid and electrified vehicle applications require implementation of high power and energy density batteries in the energy system. Especially lithium-ion batteries (LiBs) are experiencing an accelerated growth in this market volume. For cost and sustainability reasons, it is of great importance to optimize the life-time of battery usage. Therefore, it is necessary to obtain a diagnosis of the battery in terms of what is normally referred to as State of Health (SoH) [1–3].

The SoH is related to a number of factors in the battery that can be monitored and estimated [1,4], among which resistance and capacity are the most important characteristics [5,6]. Compared to capacity, which usually can be straight-forwardly measured by either constant current constant voltage (CCCV) or constant current (CC) discharge tests [7], there is less of a standardization for resistance measurements due to the complexity of the dynamic processes which it originates from. While direct current internal resistance measurements (DCIR) are more easily operated than alternating current internal resistance (ACIR) counterparts, these only provide information on the DC/Ohmic resistance of the cell [8–10]. Electrochemical impedance spectroscopy (EIS) can on the other hand – at least in theory – distinguish resistance/impedance of different processes and give information of, for example, the double layer and diffusion processes [11–13]. However, EIS measurements require specialist equipment, rendering them unpractical to merge into other more conventional testing procedures. Also, the interpretation of EIS data is often complicated, uncertain and time consuming.

As a powerful alternative, Lacey and co-workers have in a series of publications [14–18] developed a method referred to as 'intermittent current interruption' (ICI), which can straight-forwardly be used for frequent and continuous determination of a battery's internal (ohmic) resistance and diffusion resistance coefficient, which can be correlated

* Corresponding author.
E-mail address: daniel.brandell@kemi.uu.se (D. Brandell).

https://doi.org/10.1016/j.electacta.2022.140888
Received 29 November 2021; Received in revised form 15 July 2022; Accepted 19 July 2022
Available online 20 July 2022
0013-4686/© 2022 The Author(s). Published by Elsevier Ltd. This is an open access article under the CC BY license (http://creativecommons.org/licenses/by/4.0/).

to the diffusion coefficient extracted from an EIS measurement. In terms of sophistication, this puts the ICI technique between the most easily operational DCIR measurements and the fine details option of EIS measurements. In practice, ICI can generally provide information that would be obtained from EIS, but using a technique not much more complex than DCIR.

However, what the ICI method gains in simplicity and speed, it to some degree loses in detail. For example, the overall internal resistance measured by the ICI method is approximately the sum of electronic resistances in the electrode, ionic resistance in the electrolyte and charge transfer resistance at the electrode/electrolyte interface (similarly to EIS, where the diffusion kinetics are usually merged into one impendence response). Thereby, many relevant electrochemical phenomena at the electrodes or within other cell components, e.g. porous-electrode effects, transient and non-linear responses, or additional artefacts of the battery current collectors and other more peripheral components, are often not assessable.

To increase the sophistication of the ICI approach, we in this work aim to develop an approach that combines this electroanalytical experimental method with a physics-based cell model. Similar approaches have previously been beneficial for a better insight in EIS phenomena [6,19,20]. Through developments during the last decade, finite element methodology (FEM) has become a mature and valuable approach for modelling batteries for a range of cell types and geometries [21,22]. One particular advantage is that a FEM model that allows for modelling based on physical properties of the system, enable investigations of specific battery design parameters and time-dependent kinetic processes, e.g., battery ageing induced by continuous and in-situ SEI formation, etc. Such an implementation can be used for battery diagnostics by calculating resistance increase as function of SOC after a given number of cycles, while providing insight of physical and electrochemical processes of the battery to better assess the origins of the emerging cell resistances. The strength of this approach is here exemplified by analyses of commercial cylindrical 21700 Li-ion cells employing an NCA ($LiNi_{0.8}Co_{0.15}Al_{0.05}O_2$) cathode and a graphite anode.

2. The intermittent current interruption (ICI) method

2.1. Measurement technique

As mentioned above, the method used for measuring the properties of the battery cells was the intermittent current interruption (ICI) method. This technique uses a sequence consisting of first charging/discharging the battery with a constant current for a certain interval and then employing a short current interruption (for example, 1 s duration). During the current interruption, the voltage will normally first go through an almost instantaneous change (see the arrow "a" in Fig. 1) and then a considerably slower one (see the arrow "b" in Fig. 1). The influence of time-dependent sub-processes can then be calculated from the voltage response which is recorded frequently (e.g. every 0.1 s in this work) during the current interruption.

Specifically, based on the de Levie transmission line model [23], Chien et al. [16,24,25] derived that the potential change has a linear dependence with $t^{1/2}$ for a finite time after a current interruption, which is caused by the retarded capacitive behavior in a porous electrode. The same dependence can also be derived from Fick's laws, which describes diffusion processes [25]. Therefore, in both cases, the potential measurements during the current interruption can be used to extrapolate the pure resistive component that takes place at the instant of switching off the current ($t = 0$) [15]. Mathematically, the temporal evaluation of potential change for porous electrodes can thereby be interpreted as

$$\Delta E(t) = \Delta E(0) - I \times k \times \sqrt{t} \tag{1}$$

in which ΔE is the potential change, I is the applied current before interruption, t is the time after the current is switched off. k is a diffusion related parameter, identified previously as the diffusion resistance coefficient [25].

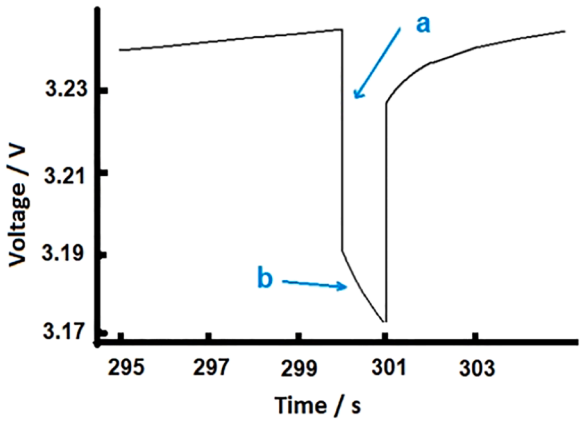

Fig. 1. Typical potential change with time during a current interruption, arrow 'a' shows the instantaneous change after the current is switched off, while arrow 'b' corresponds to the following more slowly changed potential.

Fig. 2 (a) shows the typical behavior of the potential during a one-second current interruption. The internal resistance, which includes electronic, solution and charge-transfer resistances, can thus be calculated by dividing the intercept of the linear regression of $\Delta E(t)$ against $\sqrt{t}$, i.e. $\Delta E(0)$, by the current I

$$R = -\frac{\Delta E(0)}{I} \tag{2}$$

Meanwhile, the diffusion resistance coefficient, as defined by Eq. (3), can be calculated by dividing the slope of the linear regression line by the current. Chien et al. have proved that k can be correlated to the diffusion coefficient (σ) extracted from the Warburg diffusion impedance in a conventional EIS measurement [16], and that the relationship between k and σ can be written as

$$k = -\frac{1}{I} \times \frac{\mathrm{d}\Delta E}{\mathrm{d}\sqrt{t}} \tag{3}$$

$$k = \sigma\sqrt{8/\pi} \tag{4}$$

This approach has been experimentally verified by comparing with the results from EIS in both Li-ion and Li-S systems [15,25,26].

Previously, D. Lindqvist has attempted to employ the ICI method in the investigation of a homemade coin cell, and mimic the corresponding kinetic process by establishing a FEM model [27]. Continuing upon this work, we herein aim to follow the battery ageing behavior of a commercial cylindrical 21700 cell by using the abovementioned electroanalytical method, and quantitatively interpret the origins of different ageing factors through FEM simulations.

2.2. Experimental settings

A 21700-type commercial battery employing an NCA ($LiNi_{0.8}Co_{0.15}Al_{0.05}O_2$) cathode and a graphite anode was used in this work. The battery cycling and ICI measurements were made using a PEC ACT0550 battery testing system and the cell was placed in a climate chamber at 20°C. The battery was cycled with a CCCV charge (0.5 C, 4.2 V, cutoff: 0.05 C), followed by a discharge with a constant current of 1 C till the cutoff potential of 2.5 V, and without rest between cycles. A reference performance test with ICI measurements was conducted once every 100 cycles by repeating a combination of applying a constant current for 10 min and an interruption of 1 s. Herein, a current of ± 0.48 A was used, which represents a rate of C/10 according to the capacity from the battery manufacturer. This C-rate was chosen to a moderate-to-low rate

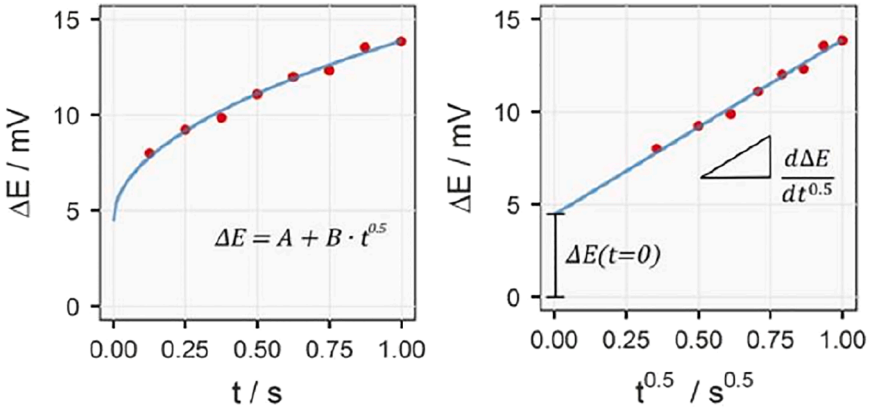

Fig. 2. Example of the ICI analysis of a current interruption experiment. Data points and the regression lines are plotted in red and blue, respectively. Δ*E* and *t* are the potential change and the time after the current is switched off. Reproduced from [24] with permission from the author.

to give an adequate amount of measurements for the resistance, as well as to be able to assume that the charge transfer resistance is ohmic. This ICI cycling protocol would in theory give 60 current interruptions per charge or discharge sequence. The data files from the ICI measurements were imported into an R environment and analyzed with a development version of the ICI analysis package [14].

3. Model establishment and validation

3.1. Pseudo two-dimensional (P2D) model establishment

3.1.1. Overview of the model and ageing factors

The most widely used model to simulate Li-ion battery behavior quantitatively is the established P2D model [28–30], in which the battery structure is simplified in a one-dimensional approach, and one extra pseudo-dimension is defined in the radial direction of the electrode material particles to address the effect of solid diffusion in the electrode. Fig. 3 represents a schematic diagram of a half cell for the investigated commercial cylindrical battery. The model is meshed with a default normal element size setting, and the extra dimension along the radial direction of the electrode particle is discretized into 10 elements. Mesh independency has been checked, showing that the simulation is convergent by using a normal and finer mesh. Geometric parameters, e.g., thickness of the electrodes, have been obtained from the analysis of opened cells (the same as used in the experimental measurement) while the properties used in the simulation for the NCA cathode, the graphite anode and the electrolyte of $LiPF_6$ in 3:7 EC:EMC were taken from the COMSOL database; see Table 1. The COMSOL database was also used for the interpolation of the OCV values for the different active materials, which originate from Hall et al. [31] for the NCA cathode and Karthikeyan et al. [32] for the graphite anode.

To simulate ageing scenarios, for instance increase in internal resistance and capacity fading, an ageing model has been established in a previous modelling work for this cell type and chemistry [33]. This takes the formation of SEI layer and metallic Li on the surface of negative graphite particles into account. Specifically, these two side reactions – SEI formation and Li plating – will consume active Li species, leading to capacity fade. Meanwhile, the formed SEI layer will increase the internal resistance directly. Compared to the SEI layer, the plated metallic Li is assumed to be highly conductive and will not increase the film resistance. Other than these, the solid products generated from the side reactions will decrease the volume fraction of the electrolyte phase, thereby further increasing the internal resistance and slowing down the diffusion kinetics in the cell. One advantage of modelling and simulation is that it is possible to assess contributions of different ageing factors, thus providing a better understanding of the origins to ageing when compared with the overall resistance values measured by experiments.

3.1.2. Governing equations

The mathematic model employed for the battery behavior is based on mass conservation and charge conservation. In the solid phase, the mass conservation of intercalated Li can be described by Fick's second law

$$\frac{\partial c_s}{\partial t} = \frac{1}{r^2}\frac{\partial}{\partial r}\left(D_s \frac{r^2 \partial c_s}{\partial r}\right) \tag{5}$$

where c_s and D_s are the concentration and diffusion coefficients of intercalated Li in the solid phase respectively, and r is the pseudo dimension along the radial direction of the electrode particles. The reaction rate of the electrochemical intercalation /deintercalation and the

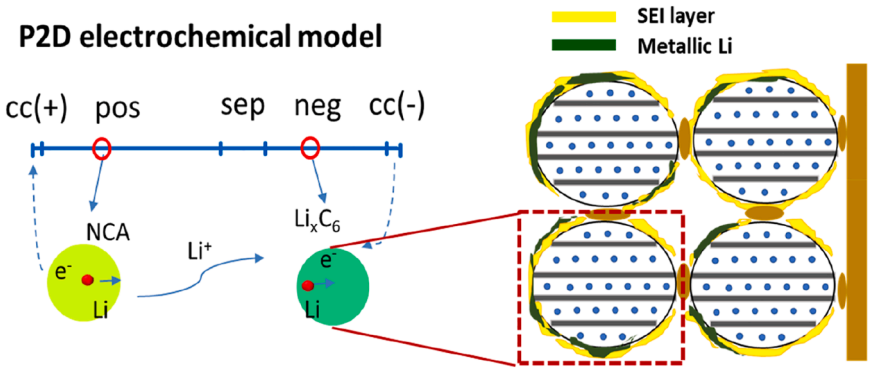

Fig. 3. Schematic diagram of the established P2D model with detailed structure of the negative electrode particles, showing SEI formation and metallic Li plating on the surface of the particles.

Table 1
Battery design specifications and parameters used in the model.

Parameters	Negative electrode	Positive electrode	Separator	Cu foil	Al foil
Design specifications					
Thickness, L (μm) [m]	75	60	10	10	20
Particle radius, rp (μm) [m]	2.5	0.25	-		
Volume fraction of electrolyte, ε_l	0.4	0.25	0.37		
Volume fraction of active material, ε_s	0.6	0.75	-		
Bruggeman coefficient [33]	1.5	2	3		
Li concentration					
Electrolyte concentration, c_l ($mol{\cdot}m^{-3}$) [c]	1200	1200	1200		
Initial solid concentration, $c_{s,initial}$ ($mol{\cdot}m^{-3}$)	28482	11328	-		
Maximum solid concentration, $c_{s,max}$ ($mol{\cdot}m^{-3}$) [c]	35603	56640	-		
Physical properties					
Electrical conductivity, σ_s ($S{\cdot}m^{-1}$) [c]	100	91	-	6.00×10^7	3.78×10^7
Li diffusion coefficient in solid phase, D_s ($m^2{\cdot}s^{-1}$) [c]	1.4532×10^{-13}	1×10^{-14}	-		
Electrolyte ionic conductivity, κ_l ($S{\cdot}m^{-1}$) [c]	$\kappa_l = \kappa_{l\,\mathrm{int}}\left(\frac{c_l}{1\,mol{\cdot}m^{-3}}\right)$				
Li ion diffusion coefficient in electrolyte, D_l ($m^2{\cdot}s^{-1}$) [c]	$D_l = D_{l,\mathrm{int}}\left(\frac{c_l}{1\,mol{\cdot}m^{-3}}\right)$				
Electrolyte activity coefficient, $f_\pm$ [c]	$f_\pm = f_{\pm,\mathrm{int}}\left(\frac{c_l}{1\,mol{\cdot}m^{-3}}\right)$				
Transference number, t_+ [c]	$t_+ = t_{+,\mathrm{int}}\left(\frac{c_l}{1\,mol{\cdot}m^{-3}}\right)$				

[m] measured from experiment
[c] from COMSOL material database

possible side reactions occurring at the interface of the electrode particles works as the boundary condition. In the liquid phase, concentrated electrolyte theory including diffusion and migration is used to describe the mass conservation of Li-ions (Eq. (6)), where ε_l is the electrolyte volume fraction, and c_l and $D_{l,\mathrm{eff}}$ are the concentration and effective diffusion coefficient of Li-ions in the liquid phase. i_l is the volumetric current density in the liquid phase, with a unit of $A{\cdot}m^{-3}$.

$$\varepsilon_l \frac{\partial c_l}{\partial t} = \nabla\cdot\left(D_{l,\mathrm{eff}}\nabla c_l\right) + \frac{i_l}{F}\times(1-t_+) \tag{6}$$

Regarding the charge conservation, the current variation in the solid phase and the potential distribution follow Ohm's law (Eq. (7)), while the local current in the liquid phase i_l can be derived from the mass transport of charged species (Eq. (8)).

$$i_s = -\sigma_{s,\mathrm{eff}}\nabla\phi_s \tag{7}$$

$$i_l = \kappa_{l,\mathrm{eff}}\left(-\nabla\phi_l + \frac{2RT}{F}\left(1+\frac{\partial \ln f_\pm}{\partial \ln c_l}\right)(1-t_+)\nabla(\ln c_l)\right) \tag{8}$$

where ϕ_s, ϕ_l are the electric potential of the solid and liquid phase and $\sigma_{s,\mathrm{eff}}$, $\kappa_{l,\mathrm{eff}}$ are the effective conductivity of solid and liquid phase, respectively. $f_\pm$ is the electrolyte activity coefficient and t_+ is the transference number for Li-ions. As boundary conditions, the electric potential at the external surface of the negative current collector is set to zero since this point is grounded in the model, and the applied charge/discharge current is defined at the end point of the positive current collector.

As depicted in Table 1, the conductivity of the electrolyte κ_l, diffusion coefficient of Li ion in the electrolyte D_l, the electrolyte activity coefficient $f_\pm$ and the transference number t_+ are defined to be functions of the Li ion concentration in the electrolyte c_l. The lookup tables from the COMSOL database is used to do the interpolation, and the results are explicitly provided in Fig. 4 [30,34–36].

3.1.3. Ageing kinetics

As mentioned, both SEI formation and Li plating are considered in the ageing model [33]. These two reactions are assumed to be electrochemical reactions and only occur in the charge process together with parallel Li intercalation and moreover only on the surface of negative electrode graphite particles. Specifically, the growth of the SEI layer is assumed to occur towards the electrolyte phase and is limited by the transport of electrons across the formed SEI layer. A first order mass transport limiting current through a Nernst boundary layer was assumed [37,38]. As a result, the surface current density caused by SEI formation ($j_{\mathrm{form,SEI}}$) can be calculated by a modified cathodic Tafel kinetics approach with limiting current density (Eq. (9)). Here, $j_{\mathrm{F,SEI}}$ is the surface current density calculated by Eq. (10). j_{lim} is the limiting current density determined by the diffusion of electrons in the formed SEI phase (Eq. (11)) while K_{SEI} is the reaction rate constant, $D_{\mathrm{e,\,SEI}}$ is the diffusion coefficient of electrons within the SEI phase, d_0 is the initial thickness of SEI layer, Δd is the increased thickness of SEI layer caused by the SEI formation during charge. The specific surface area, $S_a = \frac{3\times\varepsilon_s}{rp}$, is used to guarantee the continuity at different interfaces by projecting the volumetric change to surface flux.

$$j_{\mathrm{form,SEI}} = \frac{j_{\mathrm{F,SEI}}}{1+\frac{j_{\mathrm{F,SEI}}}{j_{\mathrm{lim}}}} = \frac{j_{\mathrm{F,SEI}}}{j_{\mathrm{lim}}+j_{\mathrm{F,SEI}}}\times j_{\mathrm{lim}} \tag{9}$$

$$j_{\mathrm{F,\,SEI}} = -n{\cdot}F{\cdot}K_{\mathrm{SEI}}c_{\mathrm{O}}^{(1-\alpha)}c_{\mathrm{R}}^{\alpha}{\cdot}\exp\left(-\frac{\alpha_{c,\,\mathrm{SEI}}F\eta}{RT}\right) \tag{10}$$

$$j_{\mathrm{lim}} = -\frac{\left(c_{\mathrm{surf}}-c_{\mathrm{bulk}}\right){\cdot}D_{\mathrm{e,SEI}}{\cdot}F}{d_0+\Delta d} \tag{11}$$

The metallic Li plating, in turn, is assumed to be a pure kinetically limited electrochemical process. The reaction rate can be calculated directly by the cathodic Tafel kinetics, Eq. (12), in which K_{Li} is the reaction rate constant. More details of the ageing model can be found in previous studies [33], while the relevant parameters are listed in Table 2, in which the conductivity of the SEI layer in the present study was adopted to fit the resistance values of equivalent experimental cells.

$$j_{\mathrm{form,\,Li}} = -n{\cdot}F{\cdot}K_{\mathrm{Li}}c_{\mathrm{O}}^{(1-\alpha)}c_{\mathrm{R}}^{\alpha}{\cdot}\exp\left(-\frac{\alpha_{c,\,\mathrm{Li}}F\eta}{RT}\right) \tag{12}$$

3.2. Model validation

COMSOL Multiphysics®, a FEM based commercial software, was used to build the model and conduct the simulations. With appropriate parameterization, the established model can be used to simulate real battery systems. To validate the model, single discharge processes at different C rates were simulated, and all simulations were implemented based on the same cylindrical battery as those used in the experimental measurements. Specifically, the nominal capacity of the battery is 4.8 Ah at 1C, with a cutoff voltage of 4.2 V for charge and 2.5 V for discharge.

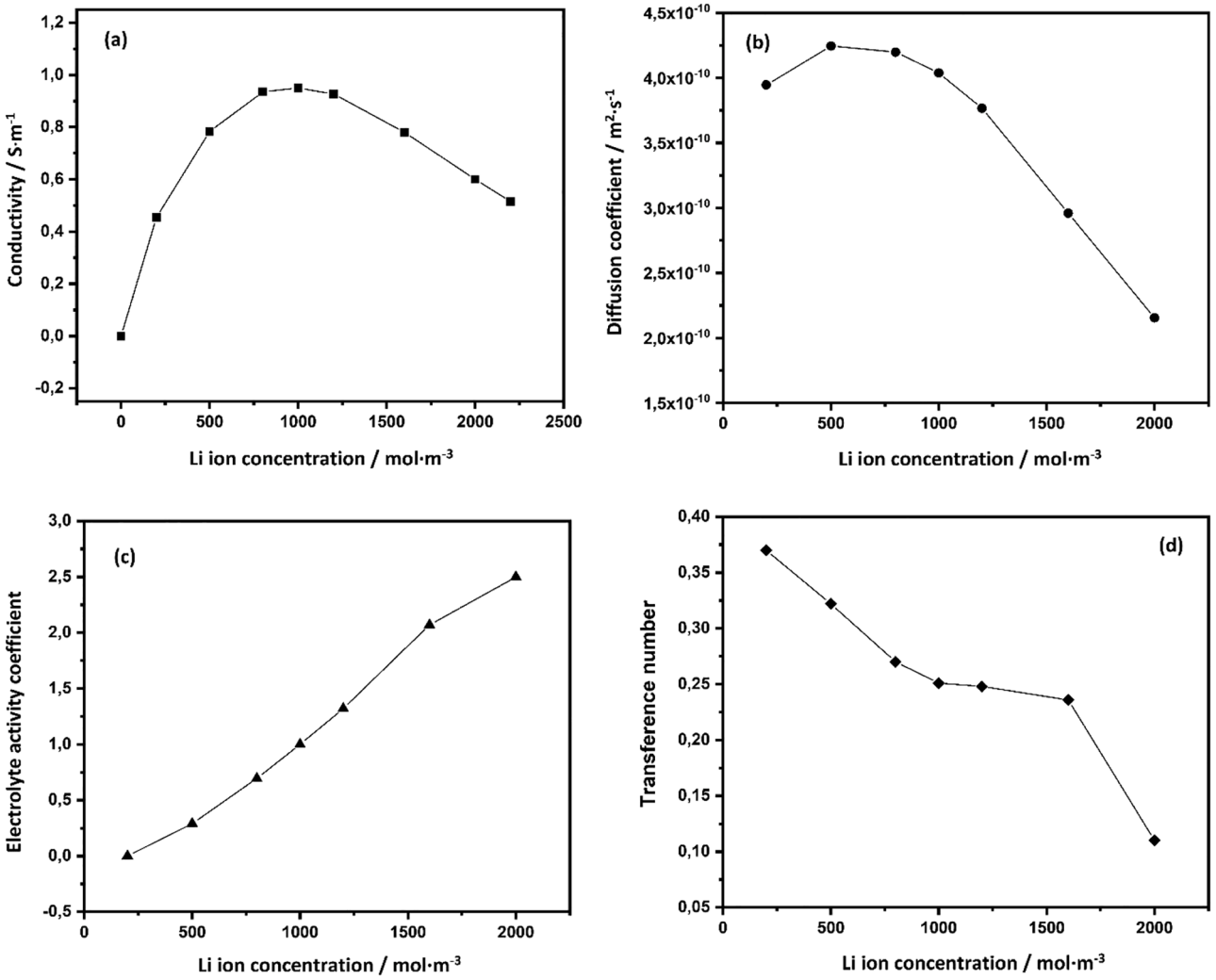

Fig. 4. (a) Conductivity, (b) diffusion coefficient, (c) electrolyte activity coefficient and (d) transference number used in the simulation as functions of the Li ion concentration.

All simulations were started from a fully charged state and went through different discharge currents until the cutoff voltage (2.5 V) were reached.

Comparison between the simulated discharge curves (lines with symbol) and the experimental results (solid lines) are shown in Fig. 5. As can be seen, the simulated discharge curves are well consistent with the experimental results for all the investigated C rates (1C, 2C, 3C, 4C). It can thus be stated that the proposed model can well mimic the electrochemical behavior of the investigated commercial cell.

3.3. Numeric implementation of ICI in the P2D model

On top of simulating the normal charge or discharge process, the ICI measurement introduces a sequence of several short current interruptions. These abrupt signal changes lead to severe difficulties to reach convergence in the numeric simulations. The conventional strategy of introducing smooth functions and using small time steps for calculation should in principle be able to solve this problem. However, since this work aims to follow the battery behavior during a long-term cycling process, including detailed ageing kinetics for the entire state-of-charge (SOC) range, there should be a one-second current interruption at least every ten minutes. If a relatively small time step is adopted for the entire simulation period, the calculation time would be impractically long. To compensate for this, a code was written in R [26] to create a sequence of range-commands that used small step lengths (0.1 s) during the current interruption, longer steps (10 s) during the constant charge/discharge current phase between the interruptions and intermediate steps (1 s) to 'bridge' between these two.

Furthermore, due to the relatively good cycling stability of the commercial cell, the investigated battery will not show any obvious ageing behavior until going through a large quantity of cycles. To thereby generate long-term cycling simulations (hundreds or even thousands of cycles) within a realistic time-frame, the ageing kinetics was accelerated by multiplying with an acceleration factor; here a value of 50 was used. This method is commonly employed in literature to simulate battery ageing [33,37,38]. By this approach, the properties related to ageing – capacity fade, resistance increase, etc. – in one simulated cycle represents the extent of these during 50 real cycles. Convergence tests were performed by varying this acceleration factor, ranging from 20 to 200.

With the abovementioned modifications, the dataset obtained from the simulation is reduced compared to the experimental results. However, 100−150 current interruptions per cycle can still be achieved, thereby providing data for a relevant comparison between these two. At each of the interruptions, the internal resistance needs to be calculated once. The dataset obtained from the cycling test will be even larger, and thus the same R code package as that used for analyzing the experimental data could easily be used to analyze also the simulation results.

Table 2
Parameters used to describe the reaction kinetics.

Parameters	Value
Reaction rate constant for Li de/intercalation, k_{neg} ($m \cdot s^{-1}$) [33]	2×10^{-11}
Reaction rate constant for Li de/intercalation, k_{pos} ($m \cdot s^{-1}$) [33]	5×10^{-10}
Anodic/cathodic transfer coefficient for Li de/intercalation, $\alpha_{a/c}$ [33]	0.5
Conductivity of SEI layer, σ_{SEI} ($S \cdot m^{-1}$)	5×10^{-5}
Initial thickness of SEI layer, d_0 (nm) [33]	3
Equilibrium potential for SEI formation, $E_{eq,SEI}$ (V vs. Li/Li^+) [33]	0.4
Cathodic charge transfer coefficient for SEI formation, $\alpha_{c,SEI}$ [33]	0.5
Reaction rate constant for SEI formation, K_{SEI} ($m \cdot s^{-1}$) [33]	$K_{SEI} = 9.58 \times 10^{-4} \times \exp\left(-\frac{E_{a,SEI}}{RT}\right)$
Activation energy for SEI formation, $E_{a,SEI}$ ($J \cdot mol^{-1}$) [33]	-15700
Molar mass of SEI, M_{SEI} ($g \cdot mol^{-1}$) [33]	160
Density of SEI, ρ_{SEI} ($kg \cdot m^{-3}$) [33]	1600
Diffusion coefficient of electrons within the SEI phase, $D_{e,SEI}$ ($m^2 \cdot s^{-1}$) [33]	$D_{e,SEI} = 1 \times 10^{-20} \times \exp\left[-\frac{E_a^{D_{e,SEI}}}{R} \times \left(\frac{1}{T} - \frac{1}{T_{ref}}\right)\right]$
Activation energy for electron diffusion, $E_a^{D_{e,SEI}}$ ($J \cdot mol^{-1}$) [33]	30000
Equilibrium potential for Li plating, $E_{eq,Li}$ (V vs. Li/Li^+) [33]	0
Cathodic charge transfer coefficient for Li plating, $\alpha_{c,Li}$ [33]	0.5
Reaction rate constant for Li plating, K_{Li} ($m \cdot s^{-1}$) [33]	$K_{Li} = 5 \times 10^{-5} \times \exp\left(-\frac{E_{a,Li}}{RT}\right)$
Activation energy for Li plating, $E_{a,Li}$ ($J \cdot mol^{-1}$) [33]	-5001
Molar mass of Li, M_{Li} ($g \cdot mol^{-1}$) [33]	6.941
Density of Li, ρ_{Li} ($kg \cdot m^{-3}$) [33]	534
Universal gas constant, R ($J \cdot mol^{-1}K^{-1}$)	8.314
Ambient temperature, T_{amb} (K)	293.15
Reference temperature, T_{ref} (K)	298.15

Before that analysis, the simulation results need to be reorganized into a proper data form, which was done by using a developed R code package [27].

4. Results and discussion

4.1. Measured and simulated initial internal resistance

Internal resistances calculated through simulations are compared with experimental datasets in Fig. 6. Here, only the resistance of the first cycle is shown, and the cycle is defined to start from a fully discharge state (capacity = 0): first to a fully charged state (capacity ca. 4.8 Ah), then followed by a discharge process until the cutoff voltage (2.5 V) is reached. The theoretical internal resistance shown in Fig. 6 (a) is calculated based on a dataset obtained from the first simulation cycle, i.e. without any ageing effect applied. The experimental result shown in Fig. 6 (b) is measured on a new battery but with 5 full cycles for stabilization, which helps to form the initial SEI layer. This corresponds to the setting of an initial SEI layer thickness of 3 nm in the established model [38–40].

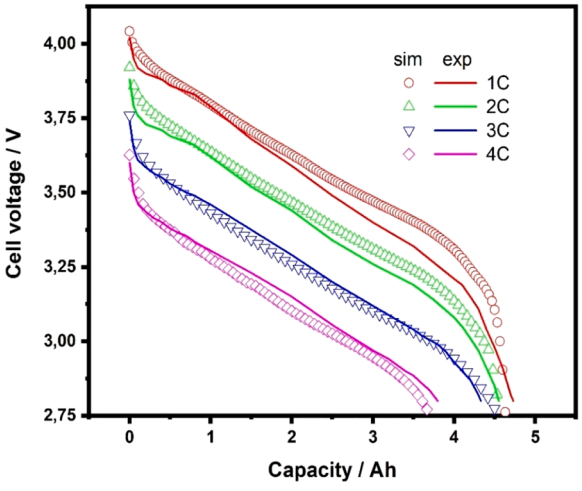

Fig. 5. Comparison of the discharge curves obtained from simulation (lines with symbol) and experimental measurements (solid lines) under different discharge rates, i.e. 1C, 2C, 3C, 4C.

The average value of the internal resistance shown in Fig. 6 is comparable between the simulation and experimental measurements, both being around 30–35 mOhm. This value agrees well with the data provided by the cell manufacturer. Moreover, the maximum of the internal resistance appears in the lower state-of-charge range for both cases. The main deviation of the simulated internal resistance compared to the measured results is instead located at the higher SOC range, i.e. the fully charged state. This can be explained by the special staging intercalation process of the graphite electrode [41,42], in which the intercalated ions group together and fill certain layers of the graphite at a given time. The model here rather assumes the graphite electrode having a lattice gas behavior, where the intercalated Li-ions spread out uniformly, while the charge transfer resistance is described through the Butler-Volmer equation. If a better fitting result is to be achieved, a more reasonable and advanced model that can describe the staging intercalation process should preferably be used. However, the current model is acceptable in this present case by predicting a relatively accurate average internal resistance for most of the SOC range.

4.2. Resistance visualization for a long-term cycling process

As discussed in the introduction, the ICI method is much faster than EIS measurements. This renders the ICI method more suitable to be used for onboard battery diagnostic, and especially for long-term cycling characterization. Fig. 7 represents the internal resistance estimated for a long-term cycling (1000 cycles) process using the ICI method. The potential response used to calculate the resistance is generated from the validated FEM model. Results after 100, 400, 700 and 1000 cycles are shown in Fig. 7 (a), and the internal resistances are drawn as function of capacity for both the charge (solid lines) and discharge (dashed lines) processes. Compared to the resistance of the first cycle, shown in Fig. 7 (a), the resistance of the cell at 50% SOC level increases from 30 mΩ to around 40 mΩ after 1000 cycles. At the same time, the capacity of the battery decreases to around 4 Ah, i.e. to 83 % compared to the initial 4.8 Ah, which is comparable with the information provided by the manufacturer.

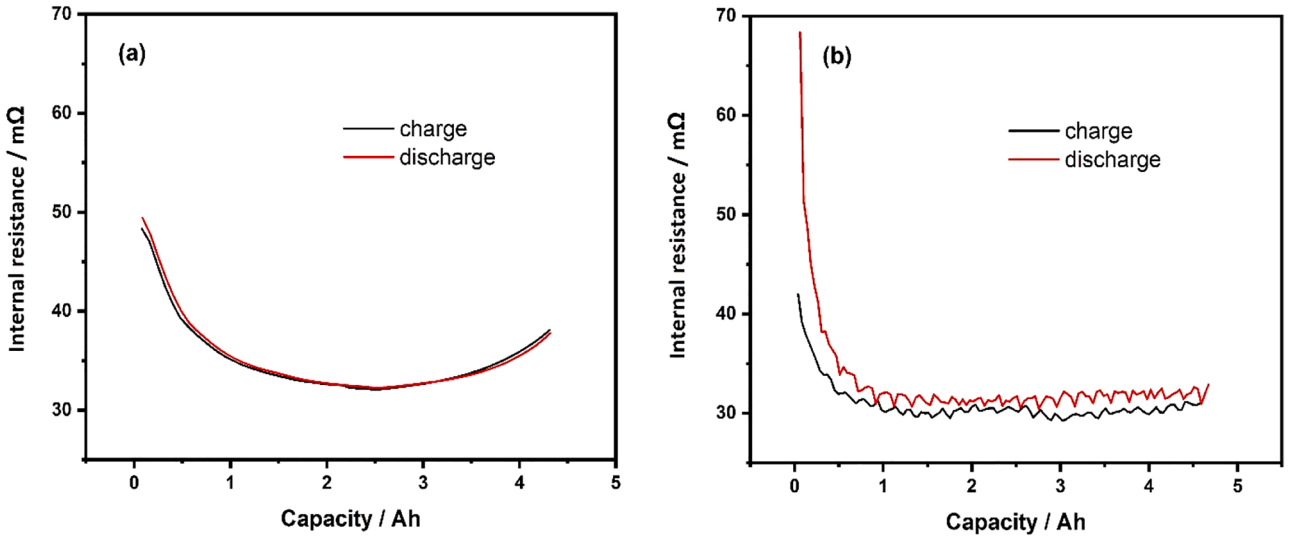

Fig. 6. Comparison of internal resistance calculated based on (a) simulation results and (b) experimental measurement, both on a commercial cylindrical 21700-type battery employing a NCA ($LiNi_{0.8}Co_{0.15}Al_{0.05}O_2$) cathode and a graphite anode.

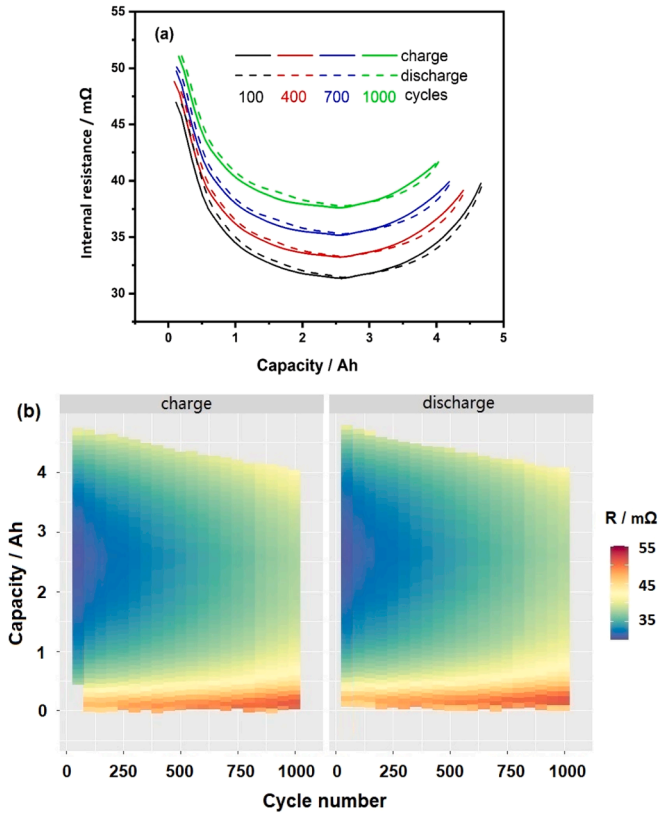

Fig. 7. (a) Simulated evolution of internal resistance through the cycling process with results after 100, 400, 700, 1000 cycles being shown; (b) 'resistance mapping' visualizing the simulated battery ageing behavior by drawing internal resistance as function of both cycle number and capacity the same time, in which the color bar represents the resistance values at each of the given points.

The calculated resistances can preferably also be plotted in a heat map, which has been referred to as 'resistance mapping' previously [14]. Compared with Fig. 7 (a), the resistance mapping, shown in Fig. 7 (b), contains more details by providing a continuous and frequently determined resistance along the entire battery cycling process. As can be seen, the resistance value of the investigated battery is relatively higher when the battery is close to a fully charged or discharged state while the minimum resistance value appears at an intermediate state. Another trend is that the internal resistance increases constantly with cycle number all the way within the investigated 1000 cycles, but there is no observed abrupt resistance increase (which usually appears right before battery failure) since the ageing kinetics in the employed model is based only on the continuous growth of SEI layer and Li plating. The resistance mapping would be even more powerful if a more advanced and complex ageing model was developed, for instance including non-linear ageing kinetics. The purpose of this present work, however, is instead to provide a basis for such a methodology through highlighting the possibility for battery diagnostic by coupling this novel electroanalytical method with a physics-based FEM model.

4.3. *Quantitative characterization of the aging kinetics*

To verify the accuracy of the model, ageing tests for 500 cycles were also conducted experimentally on commercial cells with the corresponding cell chemistry. Fig. 8 shows a quantitative comparison of the relative capacity and the internal resistance of the cell at 50 % SOC level, predicted from simulation and measured experimentally. It can be seen from Fig. 8 (a) that the capacity of the battery decreases to ca. 92 % after 500 cycles in the experimental measurements, which is consistent well with the simulation results. However, at the early stage of cycling (before 100 cycles), the trend of the measured internal resistance in Fig. 8 (b) is in worse agreement with the corresponding simulated values. The observed decrease of internal resistance in the beginning of cell operation is, however, not uncommon in similar measurements of commercial cells, although the reasons for this phenomenon has not reached a strong consensus. Groot et al. [43,44] suggested that it is caused by an initial increase of the active surface area of the electrode materials. Since this is out of the scope of current study, it will not be discussed further here. Otherwise, the following increasing trend of the internal resistance agrees well between the simulated and experimental results. The slightly lower resistance measured experimentally is reasonable and likely due to that the electrolyte chemistry is well tailored in the commercial cell and thereby render a more thin, uniform and non-resistive SEI layer than in the counterpart which has served as the basis for the SEI layer growth model.

Apart from the internal resistance, the diffusion resistance coefficient k as defined by Eq. (3) has also been extracted based on the potential response from both simulation (Fig. 9 (a)) and experiment (Fig. 9 (b)). Except from that the data obtained from the experiment is noisier, both

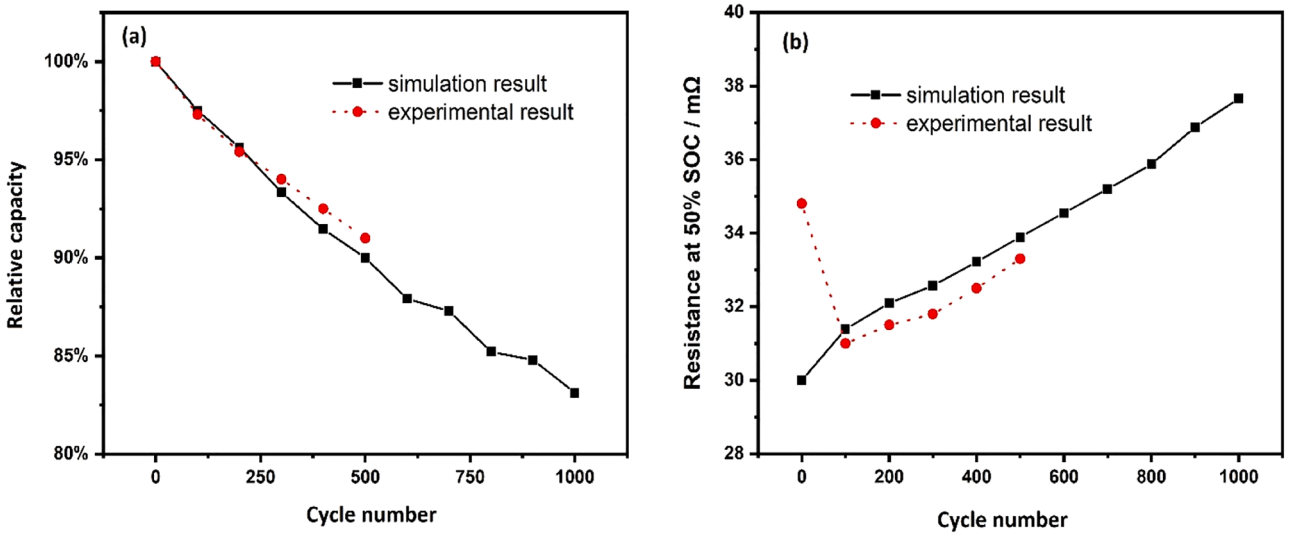

Fig. 8. Comparison between the simulation results and the experimental results, (a) shows the relative capacity and (b) shows the internal resistance of the cell at 50 % SOC level. Black lines represent the predicted values for 1000 cycles obtained from the simulation, and the red lines represent the experimentally measured results for 500 cycles.

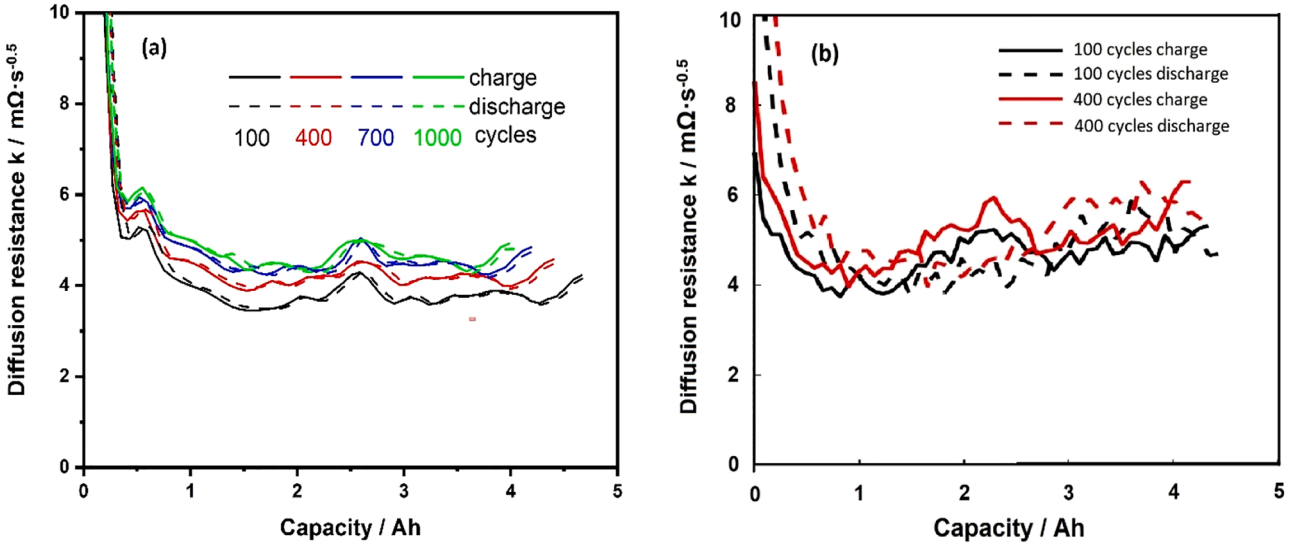

Fig. 9. Comparison of the diffusion resistance coefficient *k* values obtained from (a) simulation and (b) experiment. The simulation ran for 1000 cycles and results after 100, 400, 700, 1000 cycles are shown, while the experiment ran for 500 cycles, while results after 100 and 400 cycles are shown for comparison.

the absolute value and the changing trend of the diffusion resistance coefficient compare well between simulation and experiment. This further verifies the reliability of the established ageing model.

4.4. Characterization of different ageing factors

Battery ageing is a complex phenomenon involving different kinetic processes at interplay with each other. One advantage of the physics-based models is the possibility to extract detailed kinetic information of some of the involved sub-processes. For instance, to better assess the origins of the increased internal resistance, contributions of different factors can be compared, including the increased film resistance of the SEI layer, the decreased volume fraction of the electrolyte phase, and the consumption of active species.

Fig. 10 (a)–(c) shows the internal resistance as function of capacity after different cycle numbers (100, 400, 700, 1000 cycles); (a') (b') (c') are the corresponding resistance mapping. Specifically, Fig. 10 (a) and (a') are the results obtained by setting the resistance of the SEI film equal to zero and without considering any decrease of electrolyte volume caused by formation of solid products (SEI and metallic Li phase) from side reactions, i.e. only consumption of active Li species caused by side reactions is considered in the battery ageing. With such a model setting, the internal resistance keeps constant for the entire 1000 cycles, and only the capacity decreases accordingly.

Fig. 10 (b) and (b'), on the other hand, display results obtained without considering the volume fraction decrease of the electrolyte phase. Due to that the consumption of active species will not increase the internal resistance, as discussed above, the internal resistance increase shown in Fig. 10 (b) and (b') – as compared with (a) and (a') – is caused purely by the growth of the SEI layer. After 1000 cycles, the internal resistance at 50 % SOC increases to ca. 33 mΩ. Moreover, the increment of the resistance becomes slower with increasing cycle number. This is consistent with that the formation rate of SEI is limited by the diffusion across the formed SEI layer, i.e. further growth of SEI becomes more and more difficult when the formed SEI layer becomes thicker, resulting in self-inhibiting kinetics.

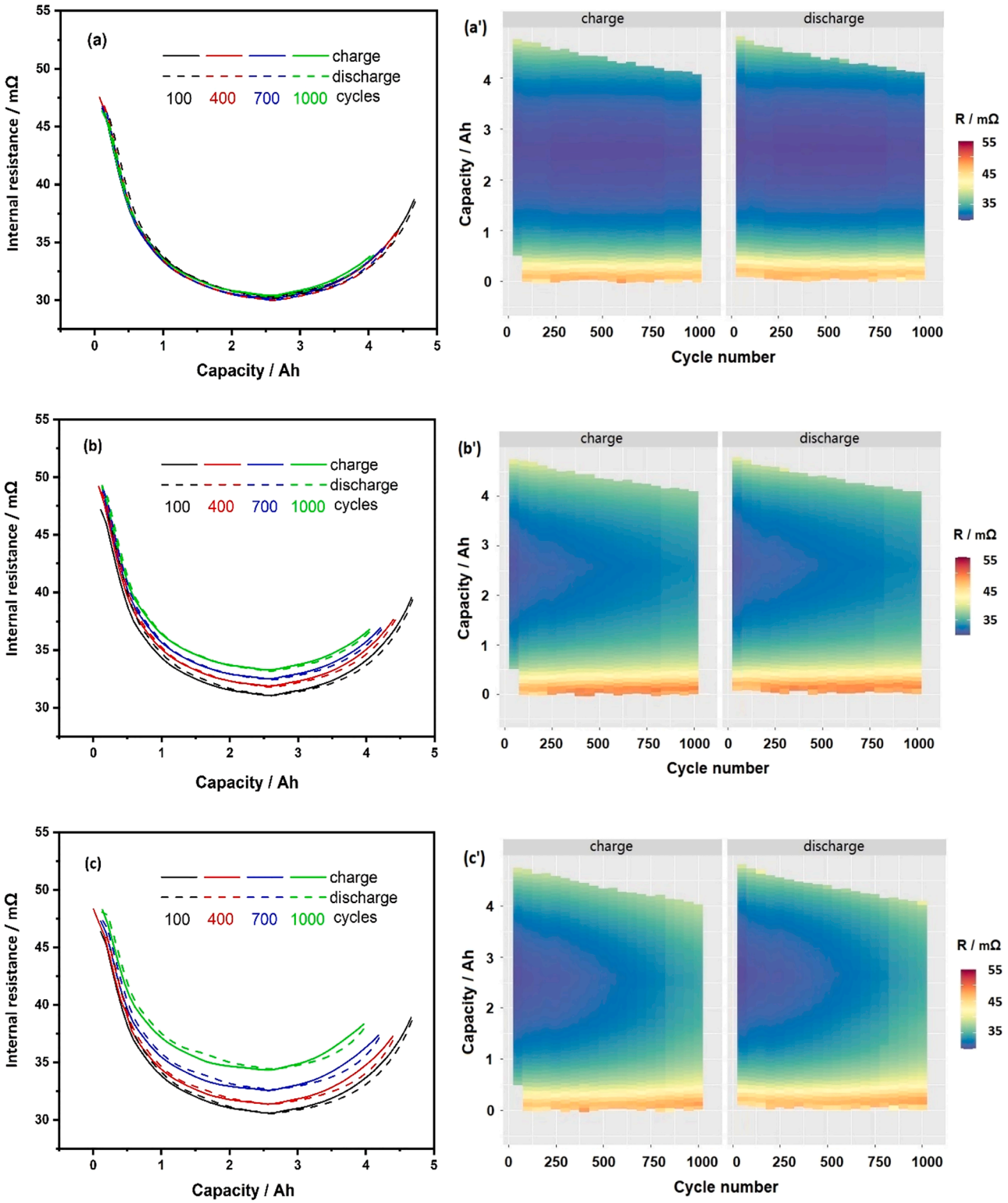

Fig. 10. (a) (b) (c) shows the internal resistance as function of capacity after different cycle numbers (100, 400, 700, 1000 cycles); (a') (b') (c') are the corresponding resistance mappings. (a) and (a') are the results obtained by setting the resistance of the SEI film equal to zero and without considering the decrease of the electrolyte volume caused by formation of solid products from side reactions. (b) and (b') are results obtained without considering the volume fraction decrease of the electrolyte phase. (c) and (c') are results calculated by setting the resistance of the SEI film equal to zero.

Fig. 10 (c) and (c') in turn present results calculated by setting the resistance of the SEI film equal to zero, thereby showing the internal resistance increase caused purely by the decrease of the electrolyte phase volume. Compared to the results in Fig. 10 (b) and (b'), the contribution of this volumetric decrease is comparatively larger than the contribution from film resistance of the SEI layer. Specifically, the volume decrease lead to an increase in the internal resistance by 5 mΩ over 1000 cycles, compared to a 3 mΩ increment in resistance by the SEI

layer. Considering that the electrolyte chemistry is usually well tailored in the commercial cell, the formed SEI layer during battery cycling can be quite thin and non-resistive. Therefore, the small increment of the internal resistance associated with SEI growth can be considered reasonable for the particular cells studied here. The comparison between different ageing factors in Fig. 10 reveals that the decreased volume fraction of the electrolyte during long-term cycling could more strongly influence battery ageing as compared to a growing resistance from the SEI layer formation, which is often regarded as the main reason for battery degradation.

In the simulation conducted, we are currently just using a constant charge/discharge current (0.1C) for the measurements. However, if for example a real drive cycle would be used as the applied condition for the model with inserted ICI measurement cycles at certain points, the real time internal resistance of the battery can easily be simulated. Before battery degradation occurs, more characteristic signals should be expected to appear, for instance abrupt or non-linear increase of the internal resistance. Meanwhile, by integrating with a physics-based model, the specific reason leading to corresponding battery degradation can be accessed, providing suggestions for optimization of battery usage, which as a final result can aid to predict battery life online. The proposed methodology by coupling a fast and flexible electroanalytical measurement with a physics-based model shows undeniable value for online battery diagnostic.

4.5. Suggestion for battery design

Another important application of modeling and simulation of Li-ion batteries is to provide directions for real device fabrication and design. Here, we have kept the shape and geometrical structure of the battery fixed while simulating the effect of different battery design parameters, e.g. porosity and particle radius of the different electrodes, on the overall internal resistance. Fig. 11 (a) and (b) show internal resistance during one cycle (first charge and then discharge) with varied porosity of the positive and negative electrodes, respectively. As can be seen from Fig. 11 (a), the internal resistance of the entire battery decreases with increased porosity of the positive electrode ($\varepsilon_{l,\mathrm{pos}}$) from 0.15 to 0.3. This is due to the fact that the electrode kinetics within this range is dominated by the electrolyte mass transport. The increase in porosity of the positive electrode therefore helps to increase the effective conductivity of the electrolyte, and as a result decreases the overall internal resistance.

A more complex trend appears in Fig. 11 (b), where the porosity of the negative electrode ($\varepsilon_{l,\mathrm{neg}}$) is increased from 0.24 to 0.48. The internal resistance turns out to first decease when $\varepsilon_{l,\mathrm{neg}}$ increases from 0.24 to 0.32, then it increases with $\varepsilon_{l,\mathrm{neg}}$ in the range from 0.32 to 0.48. This trend occurs because when $\varepsilon_{l,\mathrm{neg}}$ is relatively low (i.e., lower than 0.32), the kinetics of the negative electrode is limited by the mass transport of species in the electrolyte phase. With increasing porosity, the limiting kinetic process on the negative electrode instead becomes the active electrochemical reactions occurring on the surface of the graphite particles. Within this range ($\varepsilon_{l,\mathrm{neg}} > 0.32$), an increase of electrode porosity will decrease the volume fraction of solid materials and thus decrease the specific surface area where the electrode reactions occur.

Furthermore, the effect of particle radius of the electrode materials is also investigated. Fig. 12 (a) and (b) show the internal resistance with varying particle radii of positive and negative electrodes, respectively. The original condition employed in the simulations above is $rp_{\mathrm{pos}} = 0.25\mu$m and $rp_{\mathrm{neg}} = 2.5\mu$m. Here, both radiuses are changed stepwise by 20 %, ranging from 60 % to 120 %. It can be seen that the internal resistance decreases for both the negative and positive electrode with a decrease of the particle radius. This is due to that decreasing the particle radius will decrease the transport distance of the intercalated Li within the solid phase, and as a result decrease the reaction resistance. Moreover, the decrease in resistance is more pronounced when decreasing the particle radius of the negative electrode. This is likely because the absolute value of rp_{neg} is ten times larger than rp_{pos}. This is important from a battery design point view, where there exists a need to balance the additional cost of producing small electrode particles with the energy gained by the reduced internal resistance.

It should be pointed out that since the porosity of the electrodes and the geometrical features of the battery are fixed in these simulations, the total amount of the active material is fixed, and the capacity of the battery thereby remains unchanged when changing the particle radius. This is in contrast to the effect when changing the porosity. As can be seen from Fig. 11 (a), the increase of the positive electrode porosity will in fact decrease the effective capacity of the battery, while this will not happen if the porosity of the negative electrode is changed. This is consistent with the material balance used in this battery design; i.e., the active material of the negative electrode is designed to hold more capacity than the active material used in the positive electrode, in part because graphite is less costly than the positive material, also to leave a safe margin to avoid lithium plating. This overbalance warrants that all positive material is used effectively.

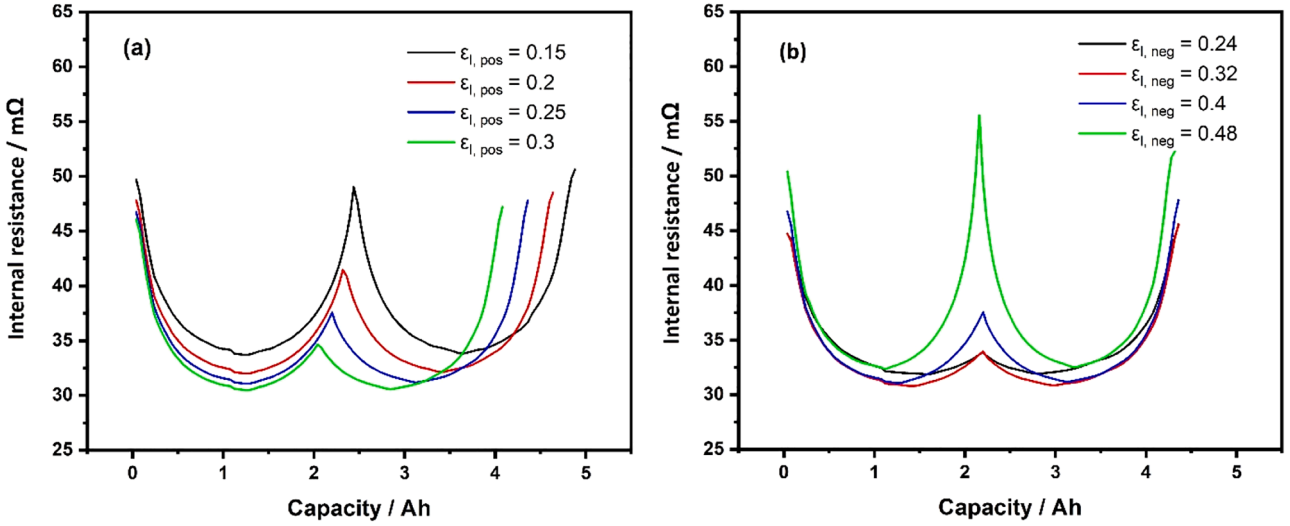

Fig. 11. Internal resistance during one cycle (first charge then discharge) with varied porosity of the (a) positive and (b) negative electrodes, respectively.

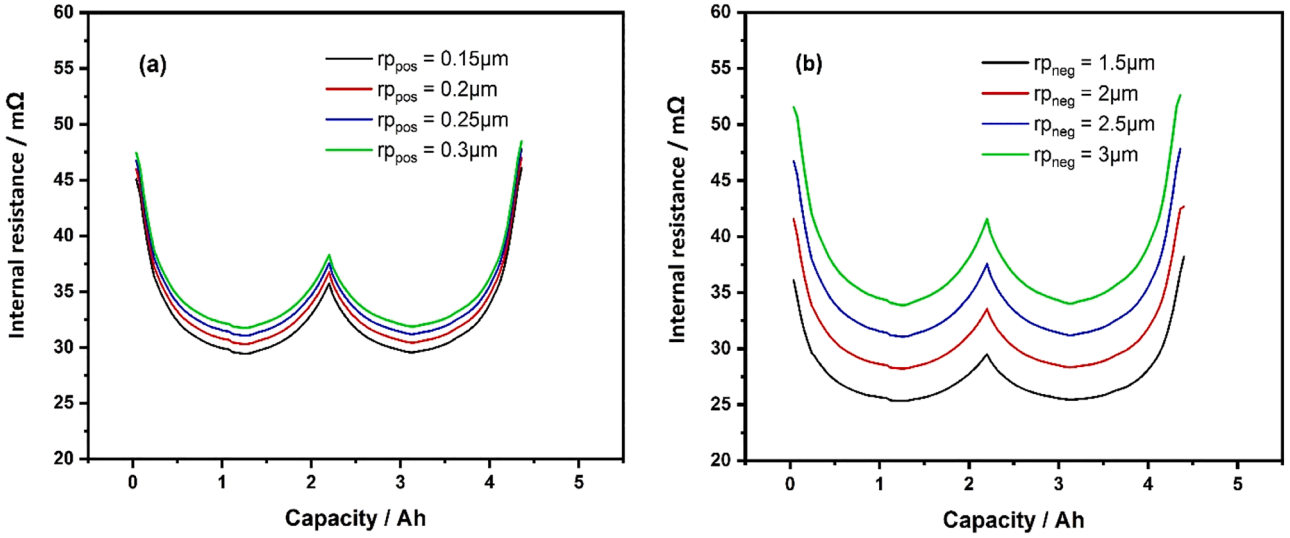

Fig. 12. Internal resistance during one cycle (first charge then discharge) with varied particle radius of (a) positive and (b) negative electrodes, respectively.

5. Conclusions

A novel electroanalytical method for online battery diagnostics, intermittent current interruption, is here employed for commercial cylindrical cells of 21700 type. By employment of an associated physics-based FEM model, the observed ageing scenario is successfully correlated with specific physical processes, for instance the SEI formation and Li plating on the surface of the graphite particles. From a long-term cycling test, the large amount of observed internal resistances obtained are visualized in heat maps, straightforwardly showing the increase of internal resistance and decrease of capacity with cycle number. Thereby, it is shown that the decrease of the electrolyte volume fraction in the porous electrodes contributes most of the investigated parameters to the resistance increase, and is also the main reason for limiting the diffusion processes in the cell during cycling. Moreover, by systematically altering different materials parameters, valuable insights into battery design appear, which further display the strength of the employed methodology.

CRediT authorship contribution statement

Litao Yin: Conceptualization, Investigation, Writing – original draft. **Zeyang Geng:** Investigation, Writing – original draft. **Yu-Chuan Chien:** Methodology, Writing – original draft. **Torbjörn Thiringer:** Writing – original draft, Supervision, Resources. **Matthew J. Lacey:** Methodology, Writing – original draft. **Anna M. Andersson:** Writing – original draft, Funding acquisition. **Daniel Brandell:** Conceptualization, Writing – original draft, Supervision, Resources.

Declaration of Competing Interest

The authors declare that they have no known competing financial interests or personal relationships that could have appeared to influence the work reported in this paper.

Data availability

Data will be made available on request.

Acknowledgment

This work has been financed by the Swedish Energy Agency through SweGRIDS. L.Y., Y.-C.C. and D.B. also acknowledge support from STandUP for Energy.

References

[1] M. Dubarry, C. Truchot, B.Y. Liaw, Synthesize battery degradation modes via a diagnostic and prognostic model, J. Power Sources 219 (2012) 204–216.
[2] A. Nuhic, T. Terzimehic, T. Soczka-Guth, M. Buchholz, K. Dietmayer, Health diagnosis and remaining useful life prognostics of lithium-ion batteries using data-driven methods, J. Power Sources 239 (2013) 680–688.
[3] Y. Merla, B. Wu, V. Yufit, N.P. Brandon, R.F. Martinez-Botas, G.J. Offer, Novel application of differential thermal voltammetry as an in-depth state-of-health diagnosis method for lithium-ion batteries, J. Power Sources 307 (2016) 308–319.
[4] A. Barré, B. Deguilhem, S. Grolleau, M. Gérard, F. Suard, D. Riu, A review on lithium-ion battery ageing mechanisms and estimations for automotive applications, J. Power Sources 241 (2013) 680–689.
[5] W. Waag, S. Käbitz, D.U. Sauer, Experimental investigation of the lithium-ion battery impedance characteristic at various conditions and aging states and its influence on the application, Appl. Energy 102 (2013) 885–897.
[6] B. Stiaszny, J.C. Ziegler, E.E. Krauß, M. Zhang, J.P. Schmidt, E. Ivers-Tiffée, Electrochemical characterization and post-mortem analysis of aged $LiMn_2O_4$–NMC/graphite lithium ion batteries part II: calendar aging, J. Power Sources 258 (2014) 61–75.
[7] X. Han, M. Ouyang, L. Lu, J. Li, Y. Zheng, Z. Li, A comparative study of commercial lithium ion battery cycle life in electrical vehicle: aging mechanism identification, J. Power Sources 251 (2014) 38–54.
[8] X. Hu, S. Li, H. Peng, A comparative study of equivalent circuit models for Li-ion batteries, J. Power Sources 198 (2012) 359–367.
[9] M. Ecker, N. Nieto, S. Käbitz, J. Schmalstieg, H. Blanke, A. Warnecke, D.U. Sauer, Calendar and cycle life study of Li (NiMnCo) O_2-based 18650 lithium-ion batteries, J. Power Sources 248 (2014) 839–851.
[10] A. Li, S. Pelissier, P. Venet, P. Gyan, Fast characterization method for modeling battery relaxation voltage, Batteries 2 (2016) 7–21.
[11] A. Barai, G.H. Chouchelamane, Y. Guo, A. McGordon, P. Jennings, A study on the impact of lithium-ion cell relaxation on electrochemical impedance spectroscopy, J. Power Sources 280 (2015) 74–80.
[12] Y. Zhang, C.-Y. Wang, X. Tang, Cycling degradation of an automotive $LiFePO_4$ lithium-ion battery, J. Power Sources 196 (2011) 1513–1520.
[13] J. Taylor, A. Barai, T. Ashwin, Y. Guo, M. Amor-Segan, J. Marco, An insight into the errors and uncertainty of the lithium-ion battery characterisation experiments, J. Energy Storage 24 (2019), 100761.
[14] M.J. Lacey, K. Edström, D. Brandell, Visualising the problems with balancing lithium-sulfur batteries by "mapping" internal resistance, Chem. Commun. 51 (2015) 16502–16505.
[15] M.J. Lacey, Influence of the electrolyte on the internal resistance of lithium−sulfur batteries studied with an intermittent current interruption method, ChemElectroChem 4 (2017) 1997–2004.
[16] Y.-C. Chien, A.S. Menon, W.R. Brant, D. Brandell, M.J. Lacey, Simultaneous monitoring of crystalline active materials and resistance evolution in lithium-sulfur batteries, J. Am. Chem. Soc. 142 (2020) 1449–1456.
[17] B. Aktekin, M.J. Lacey, T. Nordh, R. Younesi, C. Tengstedt, W. Zipprich, D. Brandell, K. Edström, Understanding the capacity loss in $LiNi_{0.5}Mn_{1.5}O_4$–$Li_4Ti_5O_{12}$ lithium-ion cells at ambient and elevated temperatures, J. Phys. Chem. C 122 (2018) 11234–11248.
[18] G. Hernández, A.J. Naylor, Y.-C. Chien, D. Brandell, J. Mindemark, K. Edström, Elimination of fluorination: the influence of fluorine-free electrolytes on the

performance of $LiNi_{1/3}Mn_{1/3}Co_{1/3}O_2$/silicon–graphite li-ion battery cells, ACS Sustain. Chem. Eng. 8 (2020) 10041–10052.
[19] S. Srivastav, C. Xu, K. Edström, T. Gustafsson, D. Brandell, Modelling the morphological background to capacity fade in Si-based lithium-ion batteries, Electrochim. Acta 258 (2017) 755–763.
[20] S. Srivastav, M.J. Lacey, D. Brandell, State-of-charge indication in Li-ion batteries by simulated impedance spectroscopy, J. Appl. Electrochem. 47 (2017) 229-236.
[21] J.M. Reniers, G. Mulder, D.A. Howey, Review and performance comparison of mechanical-chemical degradation models for lithium-ion batteries, J. Electrochem. Soc. 166 (2019) A3189–A3200.
[22] A.A. Franco, A. Rucci, D. Brandell, C. Frayret, M. Gaberscek, P. Jankowski, P. Johansson, Boosting rechargeable batteries R&D by multiscale modeling: myth or reality? Chem. Rev. 119 (2019) 4569–4627.
[23] R.D. Levie, On porous electrodes in electrolyte solutions, Electrochim. Acta 8 (1963) 751–780.
[24] Y.-C. Chien, Investigations of the performance-limiting factors in lithium-sulfur batteries (Dissertation), Uppsala University, Uppsala, Sweden, 2019.
[25] Y.C. Chien, H. Liu, A.S. Menon, W.R. Brant, D. Brandell, M.J. Lacey, A fast alternative to the galvanostatic intermittent titration technique, ChemRxiv. Cambridge: Cambridge Open Engage (2021). This content is a preprint and has not been peer-reviewed.
[26] Z. Geng, T. Thiringer, M.J. Lacey, Intermittent current interruption method for commercial lithium ion batteries aging characterization, IEEE Trans. Transp. Electrification (2021), https://doi.org/10.1109/TTE.2021.3125418.
[27] D. Lindqvist, Simulation of intermittent current interruption measurements on NMC-based lithium-ion batteries (Dissertation), Uppsala University, Uppsala, Sweden, 2017.
[28] R. Pollard, J. Newman, Transient behaviour of porous electrodes with high exchange current densities, Electrochim. Acta 25 (1980) 315–321.
[29] M. Doyle, T.F. Fuller, J. Newman, Modeling of galvanostatic charge and discharge of the lithium/polymer/insertion cell, J. Electrochem. Soc. 140 (1993) 1526–1533.
[30] M. Doyle, J. Newman, A.S. Gozdz, C.N. Schmutz, J.-M. Tarascon, Comparison of modeling predictions with experimental data from plastic lithium ion cells, J. Electrochem. Soc. 143 (1996) 1890–1903.
[31] F. Hall, S. Wußler, H. Buqa, W.G. Bessler, Asymmetry of discharge/charge curves of lithium-ion battery intercalation electrodes, J. Phys. Chem. C 120 (2016) 23407–23414.
[32] D.K. Karthikeyan, G. Sikha, R.E. White, Thermodynamic model development for lithium intercalation electrodes, J. Power Sources 185 (2008) 1398–1407.
[33] L. Yin, A. Björneklett, E. Söderlund, D. Brandell, Analyzing and mitigating battery ageing by self-heating through a coupled thermal-electrochemical model of cylindrical Li-ion cells, J. Energy Storage 39 (2021), 102648.
[34] A. Nyman, T.G. Zavalis, R. Elger, M. Behm, G. Lindbergh, Analysis of the polarization in a Li-ion battery cell by numerical simulations, J. Electrochem. Soc. 157 (2010) A1236–A1246.
[35] S. Brown, N. Mellgren, M. Vynnycky, G. Lindbergha, Impedance as a tool for investigating aging in Lithium-ion porous electrodes II. Positive electrode examination, J. Electrochem. Soc. 155 (2008) A320–A338.
[36] A. Nyman, M. Behm, G. Lindbergh, Electrochemical characterisation and modelling of the mass transport phenomena in LiPF6–EC–EMC electrolyte, Electrochim. Acta 53 (2008) 6356–6365.
[37] H. Ekström, G. Lindbergh, A model for predicting capacity fade due to SEI formation in a commercial graphite/$LiFePO_4$ cell, J. Electrochem. Soc. 162 (2015) A1003–A1007.
[38] E. Wikner, Doctor Thesis, Chalmers University of Technology, Göteborg, Sweden, 2019.
[39] D. Li, D. Danilov, Z. Zhang, H. Chen, Y. Yang, P.H.L. Notten, Modeling the SEI-formation on graphite electrodes in $LiFePO_4$ batteries, J. Electrochem. Soc. 162 (2015) A858–A869.
[40] A.A. Tahmasbi, T. Kadyk, M.H. Eikerling, Statistical physics-based model of solid electrolyte interphase growth in lithium ion batteries, J. Electrochem. Soc. 164 (2017) A1307–A1313.
[41] M.S. Dresselhaus, G. Dresselhaus, Intercalation compounds of graphite, Adv. Phys. 51 (2002) 1–186.
[42] R.B. Smith, E. Khoo, M.Z. Bazant, Intercalation kinetics in multiphase-layered materials, J. Phys. Chem. C 121 (2017) 12505–12523.
[43] J. Groot, M. Swierczynski, A.I. Stan, S.K. Kær, On the complex ageing characteristics of high-power LiFePO4/graphite battery cells cycled with high charge and discharge currents, J. Power Sources 286 (2015) 475–487.
[44] J. Groot, Doctor Thesis, Chalmers University of Technology, Göteborg, Sweden, 2014.